Chemical Science

ROYAL SOCIETY OF CHEMISTRY

EDGE ARTICLE

View Article Online
View Journal | View Issue

Cite this: *Chem. Sci.*, 2024, **15**, 11134

All publication charges for this article have been paid for by the Royal Society of Chemistry

A dual heterostructure enables the stabilization of 1T-rich $MoSe_2$ for enhanced storage of sodium ions†

Yunfeng Chao,[a] Shenghui Jia,[a] Jinzhao Li,[a] Guohui Chen,[a] Lu Liu,[a] Fei Tang,[a] Jianhua Zhu,*[a] Caiyun Wang*[b] and Xinwei Cui [a]

Received 11th April 2024
Accepted 28th May 2024

DOI: 10.1039/d4sc02400a

rsc.li/chemical-science

Electron injection effectively induces the formation of a 1T-rich phase to address the low conductivity of $MoSe_2$. Nevertheless, overcoming the inherent metastability of the 1T phase (particularly during the conversion reactions that entail the decomposition–reconstruction of $MoSe_2$ and volume expansion) remains a challenge. Guided by DFT results, we designed a composite with bimetal selenides-based heterostructures anchored on reduced graphene oxide (rGO) nanosheets (G-Cu_2Se@$MoSe_2$) to obtain stabilized 1T-rich $MoSe_2$ and enhanced ion transfer. The construction of 1T-rich $MoSe_2$ and built-in electric fields (BiEF) through electron transfer at the heterointerfaces were realized. Moreover, the rGO-metal selenides heterostructures with *in situ*-formed interfacial bonds could facilitate the reconstruction of the 1T-rich $MoSe_2$-involved heterostructure and interfacial BiEF. Such a dual heterostructure endowed G-Cu_2Se@$MoSe_2$ with an excellent rate capability with a capacity of 288 mA h g^{-1} at 50 A g^{-1} and superior cycling stability with a capacity retention ratio of 89.6% (291 mA h g^{-1}) after 15 000 cycles at 10 A g^{-1}. Insights into the functional mechanism and structural evolution of the 1T $MoSe_2$-involved dual heterostructure from this work may provide guidelines for the development of $MoSe_2$ and phase-engineering strategies for other polymorphistic materials.

1 Introduction

The increasing demand for high-mileage electric vehicles and large-scale energy-storage systems has raised concerns about the impact on natural reserves and cost of lithium metal, a key component in lithium-ion batteries (LIBs). Sodium-ion batteries (SIBs) have emerged as an alternative to LIBs owing to the abundance and low cost of sodium, high safety, and impressive electrochemical performance over a wide temperature range.[1,2] Despite sharing a similar working mechanism with LIBs, SIBs cannot directly utilize the commercial graphite anode of LIBs.[3] The development of sodium-storage anode materials is also hindered by a low rate of ion diffusion and huge volume expansion resulting from the inherently larger size of Na^+ (1.02 Å *vs.* 0.76 Å for Li^+).[4,5] Transition-metal selenides (TMS) are promising conversion-type anode materials that offer good electrochemical activity and high capacity.[2,6] Compared with transition–metal oxides or transition–metal sulfides, the larger size of Se atoms and weaker transition metal–Se bonds endow TMS with higher mobility of electrons, better ion diffusion and lower rate of volume change.[3,7] Among TMS, two-dimensional (2D)-layered $MoSe_2$ has been attracting extensive attention due to its high interlayer distance of 0.65 nm, large surface area, small bandgap of 1.1 eV and high theoretical sodium storage of 422 mA h g^{-1}.[8] However, its development is constrained by the common issues for TMS, such as low conductivity, low rate of ion diffusion, and large volume changes. These challenges affect the reaction kinetics and reversibility.

The poor electron transfer of $MoSe_2$ can be solved by phase engineering.[9] The polymorphism feature enables the transformation from a semiconductive 2H-phase to metallic-like 1T state for promoting electronic conductivity, rate of ion diffusion and electrochemical activity.[10–12] However, the Mo 4d-orbitals of 1T-$MoSe_2$ exhibit lower energy levels that are not fully filled, so the metastable 1T phase is commonly observed. Strategies such as introducing heteroatoms,[8] single atoms[13] and an intercalator[14] have been developed to realize a 1T structure in $MoSe_2$ or the analogous 2D material MoS_2 for enhanced sodium storage. All those studies have highlighted the importance and efficacy of electron injection from a donator species (P, Fe or PO_4^{3-}) to Mo atoms to achieve a balanced electron occupation in Mo 4d orbitals and promote a high content of the 1T phase. On the other hand, the formation of a composite with a second

[a]*Henan Institute of Advanced Technology, Zhengzhou University, Zhengzhou 450052, China. E-mail: jianhuazhu@zzu.edu.cn*

[b]*Intelligent Polymer Research Institute, Faculty of Engineering and Information Sciences, University of Wollongong, Innovation Campus, North Wollongong, NSW 2500, Australia. E-mail: caiyun@uow.edu.au*

† Electronic supplementary information (ESI) available: Additional information about experimental and computational details, SEM and TEM images, XPS spectra, more electrochemical results. See DOI: https://doi.org/10.1039/d4sc02400a

material having different redox potential from $MoSe_2$ can prevent the aggregation of conversion products and alleviate the mechanical stress derived from volume changes, thus benefiting the structural stability.[15,16] Metallic selenides with various bandgaps can induce spontaneous electron redistribution at heterointerfaces to generate a built-in electric field (BiEF) that enhances ion transfer.[16–18] Analogically, designing a heterostructure involving $MoSe_2$ and another selenide could be promising to overcome aforementioned drawbacks, thereby achieving stabilized 1T-$MoSe_2$ and a BiEF for promoting the transfer of electrons and ions. Such a structure has not been reported for battery materials.

Cu_2Se is an anode material with excellent sodium storage kinetics.[19,20] In particular, the β-phase Cu_2Se, with a face-centered cubic structure, possesses liquid-like Cu ions within the crystals. This feature endows it with good ionic and electronic conductivity while acting as an electron donor.[21,22] Benefiting from this unique property, β-Cu_2Se was selected to construct a bimetal selenides-based heterostructure to achieve the construction of interfacial BiEF and 1T-rich $MoSe_2$ in this work. Nevertheless, the stability of an engineered electron-injection heterostructure faces challenges due to structural evolution during the conversion reactions, which involve volume changes and decomposition–reconstruction processes.[13,23] The migration of the conversion products must be prevented during volume expansion. From this perspective, anchoring the metal selenides-based heterostructure on a suitable substrate may enhance the structural stability further by strengthening the interfacial bonds and guiding their reconstruction.[24,25] The 2D material graphene oxide (GO), with large surface area and abundant surface groups, is an ideal substrate to load metal selenides and construct interfacial bonds.[4,25] Considering all these advantages, it is reasonable to anticipate that a graphene-supported β-Cu_2Se@$MoSe_2$ heterostructure could exhibit superior sodium storage kinetics.

Herein, β-Cu_2Se was chosen as the coupling material to construct a heterostructure with $MoSe_2$. GO with abundant functional groups was introduced as the substrate. The formed GO-Cu^{2+}-MoO_4^{2-} complex in the precursor solution could guide the growth of bimetallic selenides during the hydrothermal selenylation process to form heterogenous Cu_2Se@$MoSe_2$ anchored on rGO nanosheets. DFT calculations and XPS data demonstrated the formation of 1T-rich $MoSe_2$ with improved conductivity. The improved adsorption of sodium ions and construction of BiEF at the Cu_2Se@$MoSe_2$ interface promoted the diffusion rate of Na^+. We also demonstrated that the rGO-metal selenides heterointerface played a critical part in facilitating the cyclic reconstruction of Cu_2Se@$MoSe_2$ heterostructures. As a result, an excellent sodium storage kinetic was realized in this dual-heterostructured G-Cu_2Se@$MoSe_2$ composite, as reflected by a high capacity of 288 mA h g^{-1} at 50 A g^{-1} and a high retention ratio of 89.6% after 15 000 cycles at 10 A g^{-1}.

2 Results and discussion

2.1 Density functional theory

Density functional theory (DFT) calculations were initially employed to explore the influence of β-Cu_2Se on $MoSe_2$ and to understand the possible functional mechanism of Cu_2Se@$MoSe_2$ heterostructures. As depicted in Fig. S1,† the computation model was optimized using β-Cu_2Se with an exposed (111) facet and $MoSe_2$ with an (002) facet. The selection of these exposed facets was based on previous reports.[20,26,27] The bandgap near the Fermi level in the electronic density of states (DOS) revealed the semiconductive nature of $MoSe_2$ (Fig. 1a) and the conductive feature of Cu_2Se (Fig. 1b). For Cu_2Se@$MoSe_2$ (Fig. 1c), the Mo-d was activated through the interfacial d–p–d hybridization between Cu, Se and Mo atoms. As a result, the total DOS of Cu_2Se@$MoSe_2$ at the Fermi level was much higher than that of Cu_2Se and $MoSe_2$, implying a metallic feature with excellent mobility of electrons (Fig. 1d).[18] More importantly, compared with that in Cu_2Se and $MoSe_2$, the Cu-d band and Mo-d band in Cu_2Se@$MoSe_2$ approached each other and sat closer to the Fermi energy, revealing that an electronic interaction between Cu-d to Mo-d. As displayed in the differential charge density images of Cu_2Se@$MoSe_2$ (Fig. 1e), depletion of electrons at interfacial Cu atoms and accumulation of electrons at Mo atoms were observed. Such interfacial electron transfer should enable the reorganization of the Mo 4d orbitals of $MoSe_2$ to facilitate the formation of the 1T phase and construction of BiEF.[28] The energy difference between the 2H and 1T phases decreased to 0.086 eV per atom after constructing heterostructures with Cu_2Se (Fig. S1†), which is significantly lower than the reported value for neat $MoSe_2$ (0.237 eV per atom).[14,29]

Based on analyses of the Bader charge and difference in charge density (Fig. 1e), the electron-rich Cu was capable of offering a partial electron of 0.124 e^- to Mo, resulting in the phase transition from 2H to 1T. The sodium adsorption energy was calculated based on the computational models in Fig. 1f, and was −1.22 eV for $MoSe_2$, −2.56 eV for Cu_2Se, and −1.49 eV for the $MoSe_2$ side of the Cu_2Se@$MoSe_2$ heterostructure along with −2.89 eV for the Cu_2Se side. With regard to Cu_2Se@1T-$MoSe_2$, the sodium adsorption energy was increased further to −2.09 and −3.18 eV for the 1T-$MoSe_2$ side and Cu_2Se side, respectively. Clearly, this bimetal selenides-based heterostructures could enhance the ability to capture sodium ions of Cu_2Se and 1T-rich $MoSe_2$. The enhanced adsorption energies, coupled with the BiEF generated by re-distributed electrons at the heterointerface, significantly accelerated the transfer kinetics of Na^+.[30] This theoretical analysis supports the hypothesis that the Cu_2Se@$MoSe_2$ heterostructure exhibits superior electronic conductivity and ion adsorption, indicating its potential to enhance sodium-storage performance.

2.2 Synthesis and characterization of G-Cu_2Se@$MoSe_2$

The preparation process and structural evolution of heterogeneous G-Cu_2Se@$MoSe_2$ composite are shown in Fig. 2a. In the precursor solution, the electrostatic attraction between the negatively charged surface groups on the GO surface, copper ions, and MoO_4^{2-} induced the formation of a GO-Cu^{2+}-MoO_4^{2-} complex, which facilitated the subsequent hydrothermal selenylation process for the formation of dual heterostructures. Cu_2Se@$MoSe_2$ heterostructures were directly grown on reduced graphene oxide (rGO) nanosheets to form *in situ*-generated

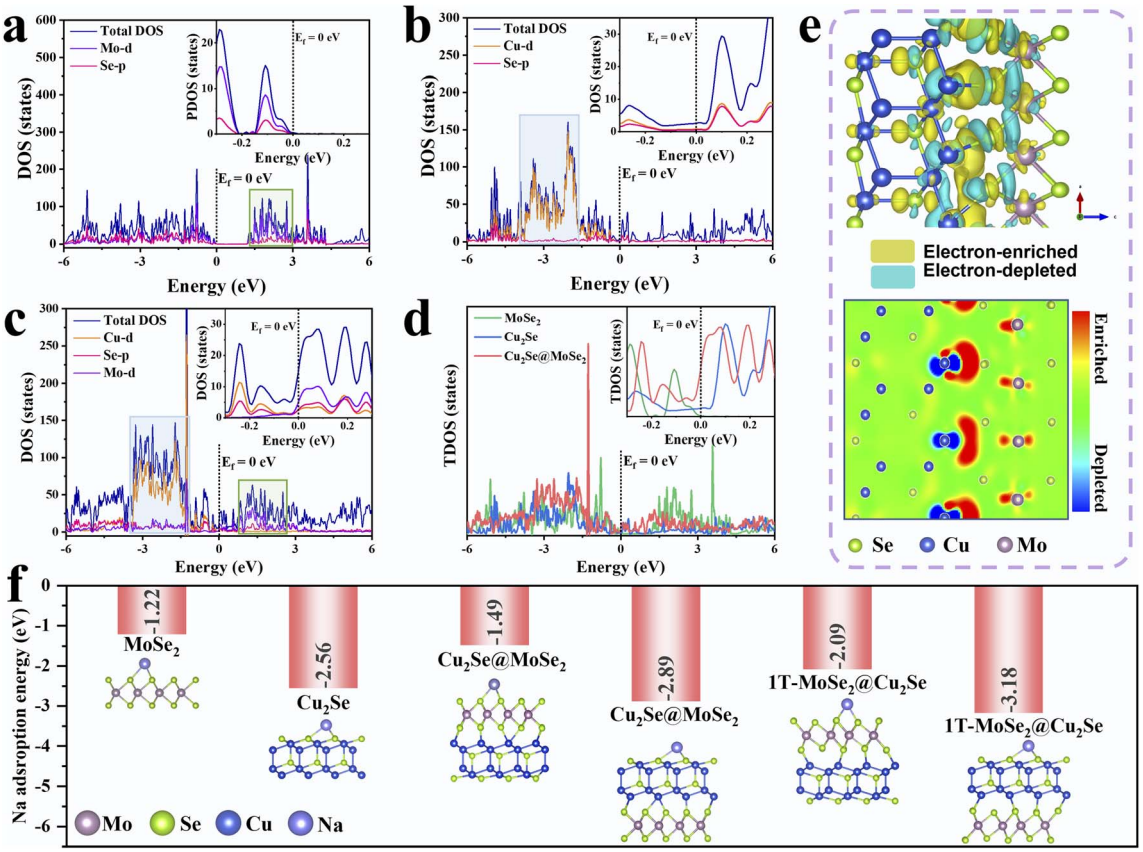

Fig. 1 Density functional theory (DFT) calculations. The partial density of states (PDOS) of (a) $MoSe_2$, (b) β-Cu_2Se and (c) Cu_2Se@$MoSe_2$. (d) The total density of states (TDOS) of $MoSe_2$, Cu_2Se and Cu_2Se@$MoSe_2$. (e) The 3D isosurface and 2D slice images showing the differential charge density of Cu_2Se@$MoSe_2$. (f) Sodium adsorption energy of the optimized models of $MoSe_2$, Cu_2Se, Cu_2Se@$MoSe_2$ and Cu_2Se@1T-$MoSe_2$.

interfacial bonds. In contrast, the Cu_2Se/$MoSe_2$ sample obtained without the use of GO (Fig. S2†) displayed large polygonal Cu_2Se nanosheets and small flocculent $MoSe_2$ with loose contact, suggesting less of a heterostructure. This observation further supported the important role of GO on guiding the growth of metal selenides to construct a Cu_2Se@$MoSe_2$ heterostructure by forming a GO-Cu^{2+}-MoO_4^{2-} complex in the precursor solution. The G-$MoSe_2$ sample displayed a hierarchical morphology with flower-like $MoSe_2$ clusters anchored on the surface of 2D rGO nanosheets (Fig. S3a and b†). As shown in the SEM images of G-Cu_2Se@$MoSe_2$ (Fig. 2b and c), the micro-sized rGO plane was fully covered with hierarchical layers. The TEM image in Fig. 2d demonstrated the uniform coverage of $MoSe_2$ layers and the existence of polygonal nanosheets. HRTEM images in Fig. 2e displays two lattice fringes with a distance of 3.3 nm and 0.67 nm, which match the (111) planes of Cu_2Se and (002) planes of $MoSe_2$ nanosheets, respectively. This result also certified the flatly decorated Cu_2Se and vertically anchored $MoSe_2$ nanosheets. Fig. 2f displays the co-existence of 1T-$MoSe_2$ and 2H-$MoSe_2$, with their positions supporting the important role of heterostructures in the formation of the 1T phase. The uniform distribution of elements C, O, Mo, Cu and Se (EDS mapping images, Fig. 2g) further evidenced the homogenous decoration of Cu_2Se and $MoSe_2$ on the rGO nanosheets.

The distinct peaks of the G-Cu_2Se@$MoSe_2$ composite in the XRD pattern (Fig. 3a) matched well with the diffraction peaks of $MoSe_2$ (JCPDS Card No. 29-0914) and β-Cu_2Se (JCPDS Card No. 65-2982). The XRD pattern of G-$MoSe_2$ in Fig. S3c† also evidenced the existence of $MoSe_2$. In the Raman spectra of Cu_2Se/$MoSe_2$ and G-$MoSe_2$ (Fig. 3b and S3d†), the main peak centered at 241 cm^{-1} was assigned to the A_{1g} peaks of 2H $MoSe_2$ and Cu_2Se.[31] With respect to G-Cu_2Se@$MoSe_2$, the representative peaks of the 1T phase emerged as J_1, J_2, E_{1g}, J_3, and E^1_{2g}, thereby confirming the formation of 1T-rich $MoSe_2$.[8,32] Besides, the weak peak at around 256 cm^{-1} could be attributed to the A_{1g} peak of the Cu_2Se nanosheets underneath.[26] The appearance of the D band (1342.2 cm^{-1}) and G band (1593.1 cm^{-1}) in G-Cu_2Se@$MoSe_2$ verified the presence of disordered carbon and graphite carbon. The higher intensity ratio of the D band to the G band ($I_D/I_G = 1.65$) than that for G-$MoSe_2$ (1.4) illustrated the abundance of defects on the rGO planes, possibly resulting from the formation of more interfacial C–Mo and C–O–M (M: Cu or Mo) bonds. The BET surface area and distribution of pore widths were characterized by N_2 adsorption–desorption isotherms (Fig. 3c). G-Cu_2Se@$MoSe_2$ and Cu_2Se/$MoSe_2$ exhibited similar type-IV isotherm plots, delivering a comparable surface area of 45.8 and 50.1 $m^2\ g^{-1}$, respectively. The slightly higher surface area of Cu_2Se/$MoSe_2$ could be attributed to the presence of flocculent $MoSe_2$ with a large exposed surface and

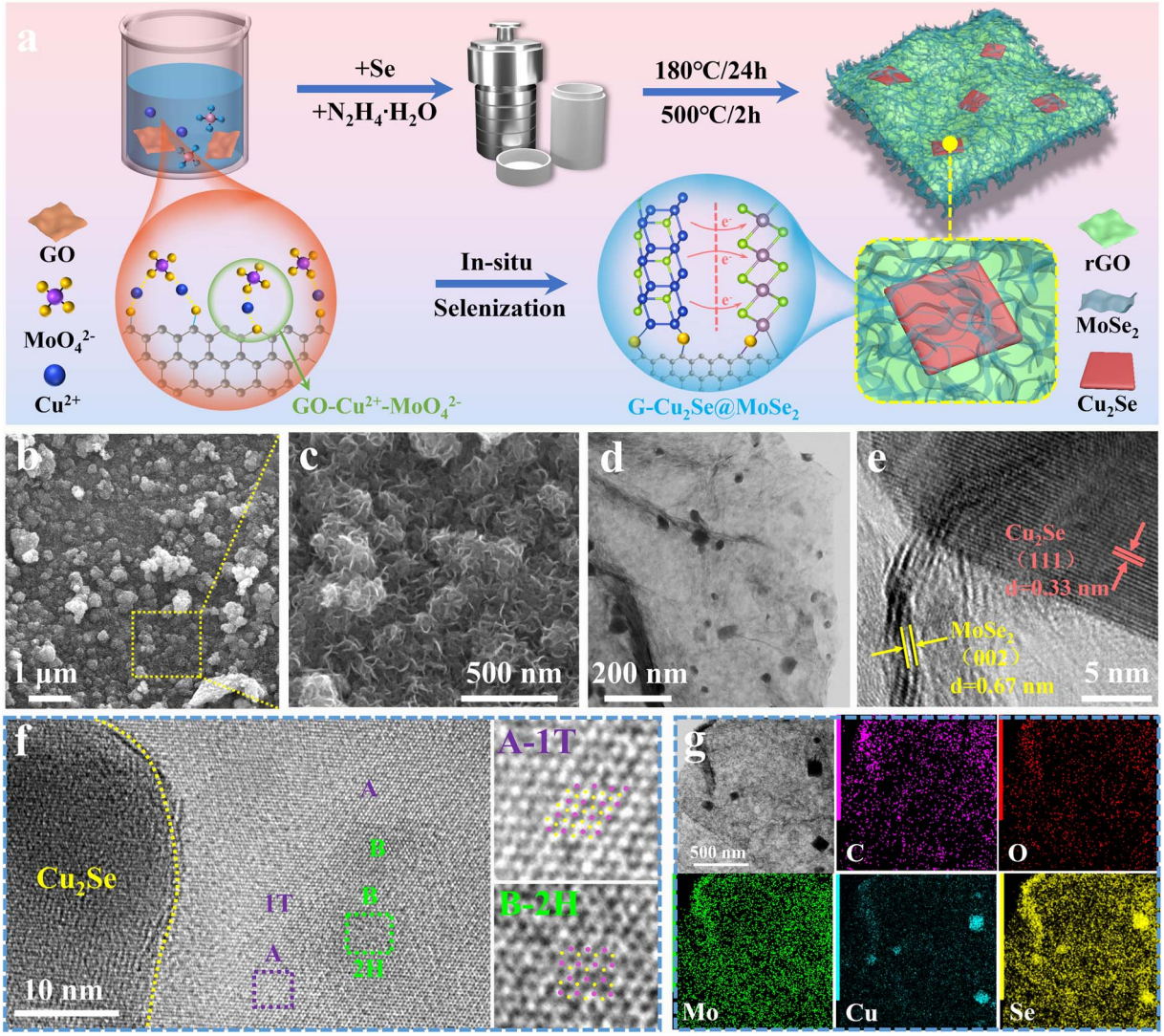

Fig. 2 Morphology of the heterogeneous G-Cu_2Se@$MoSe_2$ composite. (a) Preparation procedures of the G-Cu_2Se@$MoSe_2$ heterogeneous composite (schematic). (b and c) SEM images showing surface morphologies. TEM (d) and HRTEM (e and f) images. (g) EDS mapping images displaying the distribution of C, O, Mo, Cu and Se elements.

fewer heterostructures. In contrast, G-Cu_2Se@$MoSe_2$ possessed more covalently bonded interfaces, leading to the formation of rich heterostructures and a decrease in the exposed surface area. From this perspective, the comparable specific surface area exhibited by the heterostructure-rich G-Cu_2Se@$MoSe_2$ should be attributed to the rGO nanosheets that prevented a significant decrease in the specific surface area. The majority of pores in Cu_2Se/$MoSe_2$ had a diameter of about 2.57 nm. G-Cu_2Se@$MoSe_2$ exhibited three main pores with a diameter of 2.07, 2.57 and 7.61 nm. The hierarchical morphology and dual heterostructure of G-Cu_2Se@$MoSe_2$ may lead to the formation of multiscale pores and channels to facilitate electrolyte penetration and ion transfer.[33]

These two composites presented similar signals in the XPS spectra (Fig. S4a†). The main signals of Cu, C, Mo and Se were deconvoluted to analyze their elemental valence and chemical states. In the high-resolution C 1s spectra of G-Cu_2Se@$MoSe_2$ and G-$MoSe_2$ (Fig. 3d and S3e†), the peaks at 282.5, 284, 284.8, 286.1, 287.3, and 288.9 eV could be indexed to C–Mo, C=C, C–C, C–O–M (M: Cu or Mo), C–O and C=O bonds, respectively.[34,35] The C=C and C–C arose from rGO basal planes, while the C–O and C=O bonds were attributed to residual functional groups on the rGO surface. The presence of the C–O–M bond and C–Mo bond revealed the covalently bridged interfaces between rGO and metal atoms in selenides, which suggested the formation of rGO-metal selenides heterostructures. In the Cu 2p spectra (Fig. 3e), two weak peaks at 934.8 and 955.8 eV belonged to the Cu $2p_{1/2}$ and Cu $2p_{3/2}$ of Cu^{2+}, which could be ascribed to the interfacial C–O–Cu bond derived from the GO-Cu^{2+}-MoO_4^{2-} structure.[36] Two strong peaks centered at 932.7 and 952.6 eV contributed to the Cu $2p_{1/2}$ and Cu $2p_{3/2}$ of Cu^{+} in Cu_2Se, respectively.[26] The Mo 3d spectra in Fig. 3f and S3f† showed the peaks of Mo^{4+}, Mo^{6+} and Se 3s. The peaks at 228.8 and 231.7 eV referred to the Mo^{4+} in the 1T phase, while another two peaks at

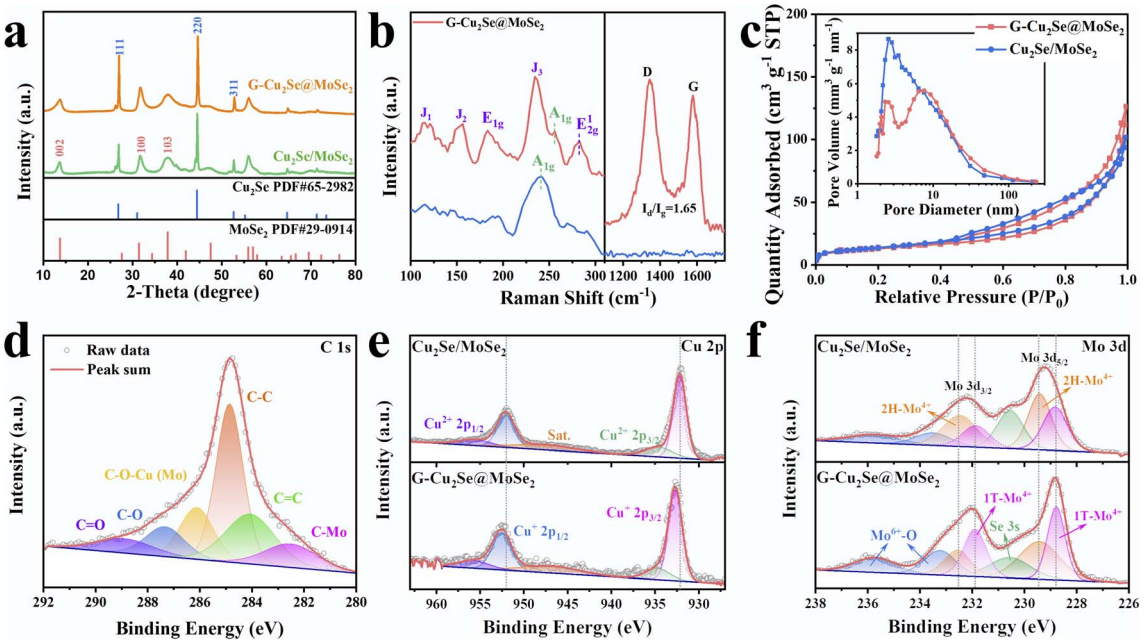

Fig. 3 Characterizations of the microstructures in $Cu_2Se/MoSe_2$ and G-$Cu_2Se@MoSe_2$ composite. (a) XRD pattern of the G-$Cu_2Se@MoSe_2$ composite. Raman spectra (b) and N_2 adsorption–desorption isotherm plots (c) of $Cu_2Se/MoSe_2$ and G-$Cu_2Se@MoSe_2$ composites. The insert in (c) is the distribution of pore sizes. (d) XPS C 1s of the G-$Cu_2Se@MoSe_2$ composite. Cu 2p (e) and Mo 3d (f) spectra of $Cu_2Se/MoSe_2$ and G-$Cu_2Se@MoSe_2$ composites.

229.4 and 233 eV represented the Mo^{4+} in the 2H state, thereby confirming the existence of 1T/2H $MoSe_2$ in these two samples.[37,38] Based on the integral area of 1T-Mo^{4+} peaks, G-$Cu_2Se@MoSe_2$ demonstrated a higher 1T-$MoSe_2$ content of 52.9%, compared with 24.7% in $Cu_2Se/MoSe_2$ and 22.1% in G-$MoSe_2$. The peak of Mo^{6+} at 232.4 and 235.6 eV could be ascribed to the partial oxidation of surface Mo atoms.[4] Compared with $Cu_2Se/MoSe_2$, the Cu^+ peaks of G-$Cu_2Se@MoSe_2$ shifted to higher binding energies, while the Mo^{4+} peaks shifted to lower binding energies, confirming electronic transfer from Cu atoms to Mo atoms at the heterointerfaces. This observation was in good agreement with the DFT results, confirming the modulation of $MoSe_2$ to achieve a higher content of the 1T phase. C 1s, Cu 2p and Mo 3d spectra also supported construction of a dual heterostructure in G-$Cu_2Se@MoSe_2$. With regard to Se 3d spectra (Fig. S4b and c†), G-$Cu_2Se@MoSe_2$ and $Cu_2Se/MoSe_2$ displayed two similar peaks of Se $3d_{5/2}$ and Se $3d_{3/2}$, which corresponded to Se^{2-} in metal selenides.[39]

2.3 Sodium storage of G-$Cu_2Se@MoSe_2$

The sodium-storage performances of G-$Cu_2Se@MoSe_2$ and $Cu_2Se/MoSe_2$ composites were first checked in half cells over a potential range of 0.1–2.5 V at a scan rate of 0.1 mV s^{-1} (Fig. 4a and S5a†). Their first three CV curves displayed three cathodic peaks and three anodic peaks at similar potential in the first scan. The peaks at 1.93 V and 1.3 V were derived from the insertion of Na^+ into Cu_2Se and $MoSe_2$ to form Na_xCu_2Se and Na_yMoSe_2, respectively.[4] The conversion from Na_xCu_2Se to metal Cu and Na_2Se contributed to the peak at ~0.92 V.[36] The peak at 0.31 V in the first scan could be assigned as the conversion of Na_yMoSe_2 and the formation of a solid electrolyte interphase (SEI).[35] It became weaker in subsequent cycles due to the irreversibility of SEI formation. The peaks at 1.5 V in the anodic sweeps resulted from the conversion reaction to form Na_xCu_2Se and Na_yMoSe_2.[26,34] Another two peaks at 1.74 and 2.05 V were related to the extraction of Na^+ to form Cu_2Se and $MoSe_2$, respectively.[40] The positions of CV peaks also matched well with the plateaus in their galvanostatic charge–discharge (GCD) curves (Fig. S5b and c†). At a current density of 0.1 A g^{-1}, the heterogeneous G-$Cu_2Se@MoSe_2$ composite delivered a higher initial discharge capacity of 600 mA h g^{-1} and a reversible capacity of 417 mA h g^{-1}, compared with 556 and 378 mA h g^{-1} for $Cu_2Se/MoSe_2$. The loss of initial capacity resulted mainly from the generation of a SEI. The higher initial coulombic efficiency for G-$Cu_2Se@MoSe_2$ (70%) compared with that of $Cu_2Se/MoSe_2$ (68%) may have been due to its smaller surface area, which consumed less Na^+ to form the SEI. It was also worthy to note that G-$Cu_2Se@MoSe_2$ possessed a smaller voltage hysteresis between charge and discharge curves, indicative of its low electrode polarization, which benefits the reversibility of the reaction.

As displayed in Fig. 4b, the sodium-storage performance was evaluated at 0.2 A g^{-1} after being activated at 0.1 A g^{-1} for three cycles. The capacity of G-$Cu_2Se@MoSe_2$ reached as high as 412 mA h g^{-1} (103.5% compared with the capacity at fourth cycle) after 250 cycles, which could be ascribed to the activation of electrodes upon cycling.[41] In contrast, it was only 295 mA h g^{-1} (93%) for $Cu_2Se/MoSe_2$. The capacity decreased slightly then increased at the initial stage, which could be attributed to electrode activation. Rate performance was

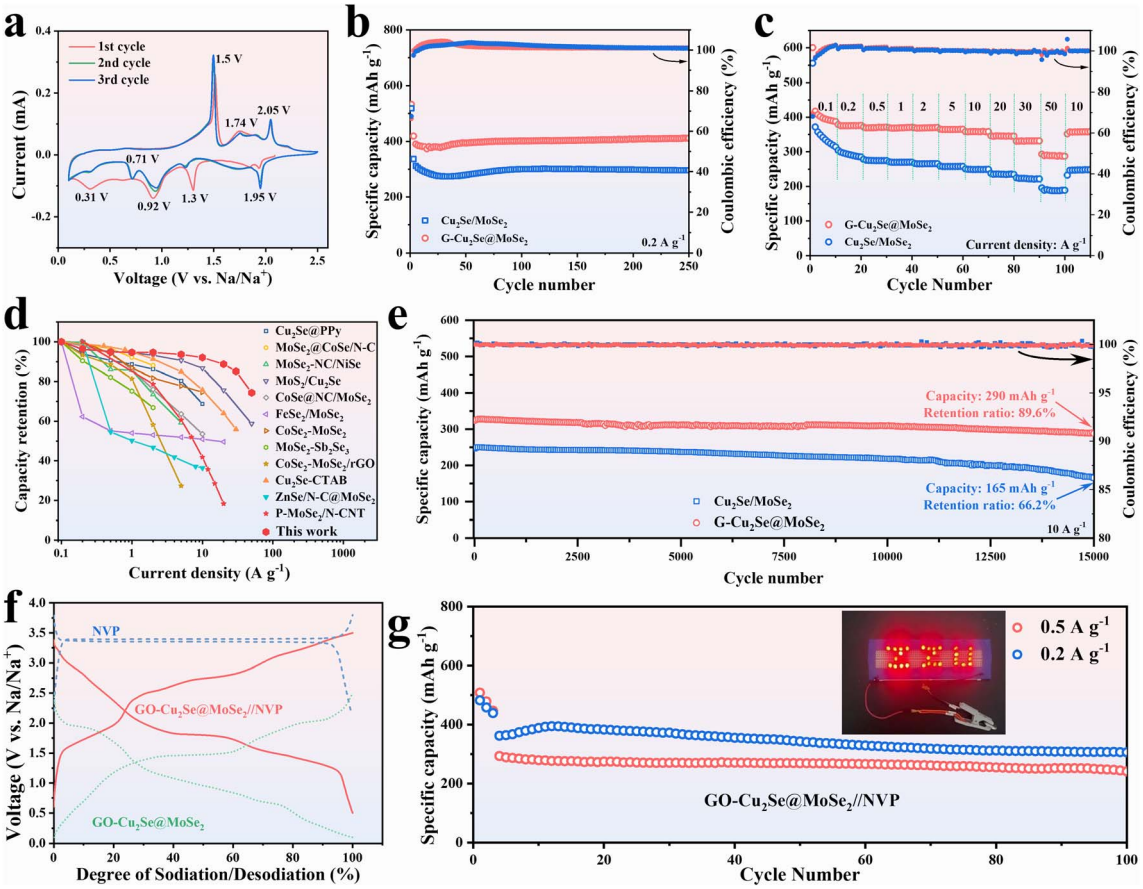

Fig. 4 Electrochemical performance in sodium ion batteries. (a) The first three cyclic voltammograms of the G-Cu_2Se@$MoSe_2$ composite at a scan rate of 0.1 mV s^{-1}. (b) Cycling performance of Cu_2Se/$MoSe_2$ and G-Cu_2Se@$MoSe_2$ at 0.2 A g^{-1}. (c) Rate capability of Cu_2Se/$MoSe_2$ and G-Cu_2Se@$MoSe_2$ composites. (d) Comparison of rate performance between G-Cu_2Se@$MoSe_2$ and reported Cu_2Se- or $MoSe_2$-based anodes. (e) Long-term cycling stability of Cu_2Se/$MoSe_2$ and G-Cu_2Se@$MoSe_2$ at a current density of 10 A g^{-1}. (f) Charge–discharge profiles of the $Na_3V_2(PO_4)_3$ (NVP) cathode, G-Cu_2Se@$MoSe_2$ anode and G-Cu_2Se@$MoSe_2$//NVP full cell. (g) Cycling performance of the G-Cu_2Se@$MoSe_2$// NVP full cell.

investigated from 0.1 A g^{-1} to 50 A g^{-1} (Fig. 4c). Heterogeneous G-Cu_2Se@$MoSe_2$ displayed much higher capacities at all currents, which were 390, 376, 370, 369, 369, 365, 359, 346, and 332 mA h g^{-1} at a current density of 0.1, 0.2, 0.5, 1, 2, 5, 10, 20 and 30 A g^{-1}, respectively. Even at a high current density of 50 A g^{-1}, a high capacity of 288 mA h g^{-1} was obtained, much higher than that obtained for Cu_2Se/$MoSe_2$ (188 mA h g^{-1}) and for G-$MoSe_2$ (93 mA h g^{-1}) (Fig. S3g†). After reverting to 10 A g^{-1}, the G-Cu_2Se@$MoSe_2$ composite maintained a higher capacity of 358 mA h g^{-1} than the 246 mA h g^{-1} for Cu_2Se@$MoSe_2$. The GCD profiles at different current densities of G-Cu_2Se@$MoSe_2$ are presented in Fig. S6.† The gradually weakened plateaus with an increase in current density revealed the domination of the capacitive process. The lower voltage hysteresis of G-Cu_2Se@$MoSe_2$ than that of Cu_2Se/$MoSe_2$ was also displayed at all current densities, evidencing its excellent rate capability. The rate performance of G-Cu_2Se@$MoSe_2$ was compared with that of other reported Cu_2Se- or $MoSe_2$-based anodes (Fig. 4d), which clearly supported the superiority of G-Cu_2Se@$MoSe_2$.[4,19,26,42–50] Such excellent rate performance could be attributed to the dual heterostructure, which increased the proportion of 1T-phase $MoSe_2$ and established interfacial BiEF for enhanced electron mobility, improved sodium adsorption, and promotion of ion transfer.

Long-term cycling stability tests were performed at 10 A g^{-1} after the rate tests (Fig. 4e). The G-Cu_2Se@$MoSe_2$ composite displayed excellent stability during the whole test, with a retention ratio of 89.6% (291 mA h g^{-1}) after 15 000 cycles. However, the Cu_2Se/$MoSe_2$ anode displayed a faster capacity fading with a retention ratio of only 66.2%. The large fluctuation in the coulombic efficiency of Cu_2Se/$MoSe_2$ also indicated its unstable conversion reactions. G-$MoSe_2$ delivered a capacity of only 194 mA h g^{-1} after 8600 cycles at 10 A g^{-1} (Fig. S3h†). The cycling performance of G-Cu_2Se@$MoSe_2$ was tested further using fresh cells (Fig. S7†), eliciting a capacity of 331 mA h g^{-1} with a retention ratio of 95.1% after 3300 cycles at 1 A g^{-1} and 323 mA h g^{-1} with a retention ratio of 94.7% after 10 000 cycles at 10 A g^{-1}. Based on the ESI in Fig. S8,† the rGO content in G-Cu_2Se@$MoSe_2$ was estimated to be 12%, while the capacity of pure rGO anodes was only 110 mA h g^{-1} at 0.1 A g^{-1}, 32 mA h g^{-1} at 50 A g^{-1}, and 42 mA h g^{-1} after 15 000 cycles at 10 A g^{-1}. These findings strongly suggested that the role of the rGO substrate lay in facilitating rapid reaction kinetics and mitigating volume changes rather than directly enhancing the

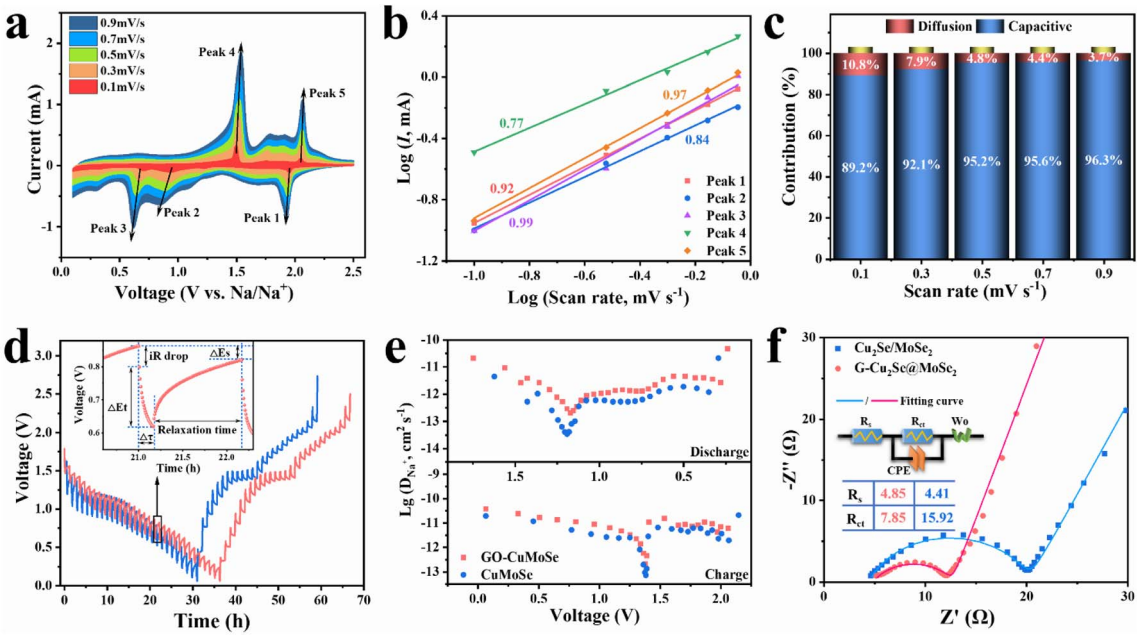

Fig. 5 Electrochemical reaction kinetics of the G-Cu_2Se@$MoSe_2$ composite. (a) CV of the G-Cu_2Se@$MoSe_2$ electrode recorded at scan rates from 0.1 to 0.9 mV s^{-1}. (b) *b* values of the marked peaks in (a) fitted from the logarithmic values of their peak currents and scan rates. (c) Contribution of a surface-capacitive process at different scan rates of the G-Cu_2Se@$MoSe_2$ electrode. (d) GITT curves of G-Cu_2Se@$MoSe_2$ and Cu_2Se/$MoSe_2$ composites (inset is an enlarged cycle). (e) Diffusion coefficient of Na^+ during charge and discharge processes. (f) Nyquist plots of G-Cu_2Se@$MoSe_2$ and G-Cu_2Se/$MoSe_2$ composites (inset is the model of an equivalent circuit and fitted values of R_s and R_{ct}).

capacity. Unequivocally, the outstanding sodium-storage performance of the G-Cu_2Se@$MoSe_2$ composite could be attributed to the construction of dual heterostructures. The bimetal selenides-based heterostructure limited the aggregation of conversion products and accommodated the expansion stress, while the rGO-metal selenides heterostructure facilitated the reconstruction of a bimetal selenides-based heterostructure, leading to stabilization of 1T-rich $MoSe_2$ and BiEF.

To evaluate the practical application of the G-Cu_2Se@$MoSe_2$ composite further, full SIB batteries coupled with $Na_3V_2(PO_4)_3$ (NVP) cathodes were assembled. NVP cathodes exhibited a plateau of about 3.35 V in half cells with metal sodium as counter electrodes (Fig. 4f) and delivered a high specific capacity of 89.3 mA h g^{-1} after 100 cycles at 1 A g^{-1} (Fig. S9a†). With regard to G-Cu_2Se@$MoSe_2$//NVP full cells, a voltage window of 0.5–3.5 V was chosen to perform electrochemical tests. Based on the weight of active materials (G-Cu_2Se@$MoSe_2$) in anodes, a high specific capacity of 335, 283 and 190 mA h g^{-1} was obtained at 0.5, 1 and 2 A g^{-1}, respectively (Fig. S9b†). The calculated energy density of the full cell could reach as high as 144.7 W h kg^{-1}. After 100 cycles (Fig. 4g), the full cell could deliver a reversible capacity of 306 mA h g^{-1} (84.5%) at 0.2 A g^{-1} and at 241 mA h g^{-1} (82.2%) at 0.5 A g^{-1}. The inset image in Fig. 4g demonstrates a "ZZU" pattern composed by 29 LED bulbs that had been lit-up by a fully charged G-Cu_2Se@$MoSe_2$// NVP cell, thereby proving its practical potential.

2.4 Reaction kinetics of G-Cu_2Se@$MoSe_2$

The electrochemical reaction kinetics of the G-Cu_2Se@$MoSe_2$ composite were investigated by analyzing the capacitive contribution, impedance properties and ion diffusivity. The CV curves of G-Cu_2Se@$MoSe_2$ and Cu_2Se@$MoSe_2$ composites at various scan rates were collected and are shown in Fig. 5a and S10a,† respectively. The marked five peaks were selected to analyze the capacitive contributions on the basis of the power-law relationship ($i = avb$) between peak current (i) and scan rate (v).[47] A *b* value of 1 indicates a surface-capacitive dominated electrochemical process. A *b* value of 0.5 denotes a diffusion-controlled process. By fitting the linear slopes of log (i) *versus* log (v) (Fig. 5b), all values of *b* were determined in the range of 0.77–1, suggesting that the discharge/charge processes of G-Cu_2Se@$MoSe_2$ was mainly controlled by surface-capacitive behavior.[34] In contrast, the slightly lower *b* values for Cu_2Se/$MoSe_2$ (Fig. S10b†) indicated a lower capacitive contribution. Then, the contribution of surface-capacitive processes at each scan rate (v) was calculated through the equation $i = k_1v + k_2v^{0.5}$, where k_1v and $k_2v^{0.5}$ are the sections of capacitive and diffusion processes, respectively.[51] Unsurprisingly, G-Cu_2Se@$MoSe_2$ displayed a higher capacitive contribution at all scan rates (Fig. 5c and S10c†). For example, the capacitive contribution for G-Cu_2Se@$MoSe_2$ and Cu_2Se/$MoSe_2$ (Fig. S11†) was 92.1% and 89.6% at 0.3 mV s^{-1}, respectively. The higher contribution of the capacitive process in G-Cu_2Se@$MoSe_2$ could enable fast reaction kinetics and, thus, excellent rate performance.

Ion diffusion coefficients (D) were studied by the galvanostatic intermittent titration technique (GITT) as presented in Fig. 5d. According to eqn (S1†),[52] plots of D values during charge and discharge processes are given in Fig. 5e. Heterogenous G-Cu_2Se@$MoSe_2$ possessed a higher diffusion coefficient of Na^+ during the entire electrochemical reaction. This excellent Na^+

transfer kinetics could have mainly resulted from the enhanced adsorption energy of Na^+ and the BiEF at the heterointerfaces of Cu_2Se@$MoSe_2$. The kinetic data of G-$MoSe_2$ were also collected (Fig. S12†) and showed a low contribution of surface capacitive process at all scans and poor ion diffusivity. These sluggish reaction kinetics were in good accordance with the poor rate performance of G-$MoSe_2$ (Fig. S3g†), further emphasizing the crucial role of heterostructures. Nyquist plots, an equivalent circuit and fitted results of fresh cells are presented in Fig. 5f. The labels of R_s, R_{ct}, CPE and Wo used in the equivalent circuit represent contact resistance, charge transfer resistance, constant phase element and Warburg impedance, respectively.[53] The G-Cu_2Se@$MoSe_2$ composite displayed a smaller semicircle in the high-frequency region with a lower charge transfer resistance (R_{ct}) of 7.85 Ω than that for Cu_2Se/$MoSe_2$ (15.92 Ω). Conductive rGO nanosheets, 1T-phase rich $MoSe_2$ and interfacial bonds were likely the main reasons. Warburg factors were acquired by fitting the linear slopes of Z' *versus* $\omega^{-1/2}$ in Fig. S13a.† [43] According to eqn (S2),† the smaller Warburg factor (σ) for G-Cu_2Se@$MoSe_2$ indicated a faster diffusion rate of Na^+ than that for the control sample. These results confirmed the exceptional Na^+ transfer kinetics of G-Cu_2Se@$MoSe_2$, which could be ascribed to improved sodium adsorption and interfacial BiEF. The impendence property of G-Cu_2Se@$MoSe_2$ upon cycling was also investigated (Fig. S13b†). The R_{ct} decreased to about 4.07 after 20 cycles and retained almost no change at 50 cycles. On the other hand, the Warburg factor decreased to 25.7 at 20 cycles and 18.8 at 50 cycles, indicating the continuous increase of ion diffusivity along cycling, which could be attributed to electrode activation creating more ion-diffusion channels.[54] This activation process also reconstructed the electrode structure to increase the amount of ion-accessible active materials, thereby enhancing the capacity during the initial cycling stage of fresh G-Cu_2Se@$MoSe_2$ anodes, as observed in Fig. S7.†

2.5 Structural evolution and reaction mechanism

The stability of dual heterostructure and 1T-rich $MoSe_2$ during cycling tests were critical for the cycling performance of G-Cu_2Se@$MoSe_2$. To investigate the structural evolution, cycled cells were disassembled to examine the active materials by TEM and XPS. HRTEM images of G-Cu_2Se@$MoSe_2$ with the corresponding selected area electron diffraction (SAED) pattens at 0.1 V and 2.5 V are presented in Fig. 6a and b, respectively. The

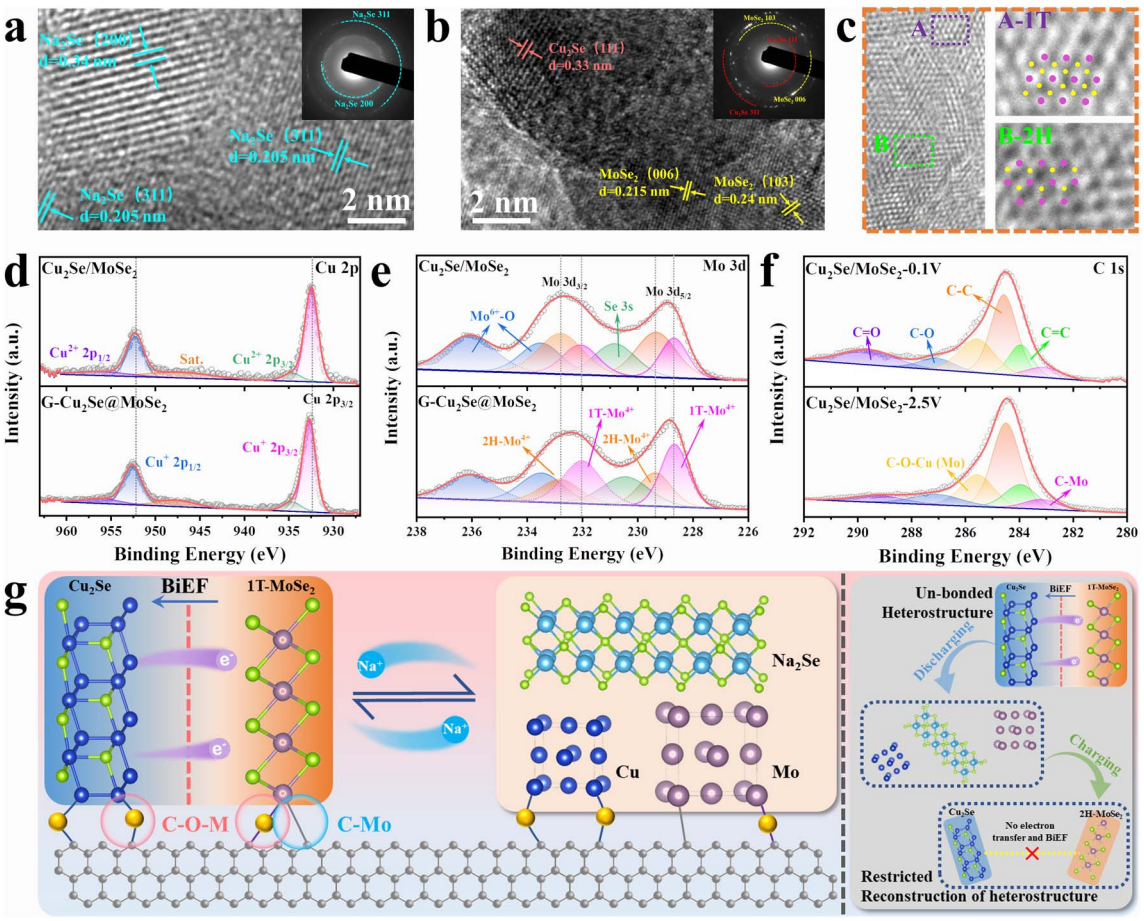

Fig. 6 Structural evolution of G-Cu_2Se@$MoSe_2$. TEM images and corresponding SAED patterns of cycled G-Cu_2Se@$MoSe_2$ anodes that disassembled at 0.01 V (a) and 2.5 V (b). HRTEM images of cycled G-Cu_2Se@$MoSe_2$ showing the presence of 1T/2H $MoSe_2$. Cu 2p (d) and Mo 3d (e) spectra of cycled Cu_2Se/$MoSe_2$ and G-Cu_2Se@$MoSe_2$ anodes. (f) C 1s spectra of cycled G-Cu_2Se@$MoSe_2$ anodes at 0.01 V and 2.5 V. (g) Reaction mechanism of G-Cu_2Se@$MoSe_2$ for stabilizing the reconstruction of the Cu_2Se@$MoSe_2$ heterostructure and 1T-rich $MoSe_2$.

lattices observed at 0.1 V were the (311) and (200) planes of Na_2Se. They matched well with the SAED patterns, indicating completion of the conversion reaction. At 2.5 V, the lattice distance of 0.215 and 0.24 nm belonged to the 006 and 103 planes of $MoSe_2$, respectively. Another crystal lattice with a *d*-spacing of 0.33 nm was the (111) plane of Cu_2Se. They were also in good agreement with SAED patterns, demonstrating good recovery of metal selenides after desodiation. EDS mapping images in Fig. S14† confirmed the uniform distribution of Cu, Mo and Se elements in the cycled G-Cu_2Se@$MoSe_2$ composite, evidencing the reconstruction of the Cu_2Se@$MoSe_2$ heterostructure. In addition, HRTEM images in Fig. 6c demonstrated the co-existence of 1T-$MoSe_2$ and 2H $MoSe_2$. The Raman spectrum in Fig. S15† also displays the representative peaks of 1T $MoSe_2$, revealing the well-preserved 1T phase in the cycled G-Cu_2Se@$MoSe_2$ anode. The Cu 2p spectra in Fig. 6d and Mo 3d patterns in Fig. 6e were similar to their initial states. The shifting of Mo^{4+} peaks to lower energies and Cu^{+} to higher energies could be detected in the G-Cu_2Se@$MoSe_2$ composite, illustrating the preservation of 1T-rich $MoSe_2$. Interestingly, the portion of 1T-$MoSe_2$ in G-Cu_2Se@$MoSe_2$ was increased slightly to 62.5%, while the control sample remained unchanged. Moreover, the presence of C–O–M (M: Cu or Mo) and C–Mo bonds in the C 1s spectra of G-Cu_2Se@$MoSe_2$ at 0.1 V and 2.5 V (Fig. 6f) confirmed their stability during the conversion reaction, which facilitated the reconstruction of heterostructures. This finding could also explain the absence of Cu and Mo in the TEM image of G-Cu_2Se@$MoSe_2$ at 0.1 V. The generated Cu and Mo should be fixed on the surface of rGO and coverage by Na_2Se. This result, combined with TEM data, could strongly support that the dual heterostructure ensured the excellent stability of the Cu_2Se@$MoSe_2$ heterostructure to facilitate the reconstruction of 1T-$MoSe_2$ upon cycling.

The reaction mechanism and structural evolution of dual heterostructures in G-Cu_2Se@$MoSe_2$ is summarized and illustrated in Fig. 6g. The electron transfer generated at the heterointerfaces contributes to the formation of BiEF and a high content of 1T phase in $MoSe_2$. Crucially, the stability of interfacial C–O–M (M: Cu or Mo) and C–Mo bonds at the rGO-metal selenides heterointerfaces is essential during the conversion process. This stability can effectively hinder the unrestrained growth and migration of the formed metal agglomerations, thereby promoting the subsequent reconstruction of Cu_2Se@$MoSe_2$ heterostructures throughout the charging process. This action further stabilizes the cyclic formation of interfacial BiEF and 1T-rich $MoSe_2$. In contrast, the un-bonded Cu_2Se@$MoSe_2$ heterostructures experience unrestricted growth of conversion products, ultimately leading to the degradation of heterostructures and a decreased content of 1T phased $MoSe_2$.[55–57] Consequently, it can be inferred that the interfacial bonds between rGO and metal selenides have a pivotal role in facilitating the transfer of electrons and ions during long-term charging/discharging cycles. This functional mechanism highlights the crucial interactions between the dual heterostructures in the G-Cu_2Se@$MoSe_2$ composite, which holds pivotal importance for the prospective design and development of bimetal selenides-based heterostructures.

3 Conclusions

To summarize, a dual-heterostructured G-Cu_2Se@$MoSe_2$ composite was developed through a facile hydrothermal process by leveraging the GO-Cu^{2+}-MoO_4^{2-} complexes in the precursor. Electron transfer at the Cu_2Se@$MoSe_2$ interface, confirmed by DFT and XPS, induces the formation of the 1T phase in $MoSe_2$, improving conductivity and creating a built-in electric field to enhance ion transfer. Moreover, the stable interfacial bonds between rGO and metal selenides immobilize the conversion products, thereby facilitating the reconstruction of heterostructures during cyclic conversion reactions. Consequently, the 1T-rich $MoSe_2$ and BiEF are maintained, enabling the continuous enhancement of electron and ion transfer during long-term cycling processes. As a result, the G-Cu_2Se@$MoSe_2$ composite delivered excellent electrochemical performance, such as a high capacity of 390 mA h g^{-1} at 0.1 A g^{-1}, excellent rate performance of 288 mA h g^{-1} at 50 A g^{-1}, and long-term cycling stability with a capacity retention ratio of 89.6% after 15 000 cycles at 10 A g^{-1}. We also revealed the working mechanism of the 1T $MoSe_2$-involved heterostructure and the structural evolution during conversion reactions. The insights from this work may offer valuable guidelines for the development of conversion materials for sodium ion batteries.

Data availability

The data underlying this study are available in the ESI.†

Author contributions

Y. C.: conceptualization, investigation, experimental methodology, and writing – original draft. S. J.: investigation, synthetic methodology, and writing – original draft (synthesis). J. L.: validation, data curation, and visualization. G. C., L. L. and F. T.: investigation. J. Z.: conceptualization, supervision, and writing – review and editing. N. H.: conceptualization and supervision. C. W.: conceptualization and supervision.

Conflicts of interest

There are no conflicts of interest to declare.

Acknowledgements

The authors gratefully acknowledge the financial support from National Natural Science Foundation of China (No. 52202119 and 52272242), Natural Science Foundation of Henan Province (No. 242300421432) and fellowship of China Postdoctoral Science Foundation (No. 2022TQ0283).

Notes and references

1 P. K. Nayak, L. Yang, W. Brehm and P. Adelhelm, *Angew. Chem., Int. Ed.*, 2018, **57**, 102–120.

2 H. Kim, H. Kim, Z. Ding, M. H. Lee, K. Lim, G. Yoon and K. Kang, *Adv. Energy Mater.*, 2016, **6**, 201600943.
3 Y. Gong, Y. Li, Y. Li, M. Liu, Y. Bai and C. Wu, *Small*, 2023, **19**, 2206194.
4 Y. Xu, X. Liu, H. Su, S. Jiang, J. Zhang and D. Li, *Energy Environ. Mater.*, 2022, **5**, 627–636.
5 J. Y. Hwang, S. T. Myung and Y. K. Sun, *Chem. Soc. Rev.*, 2017, **46**, 3529–3614.
6 M. Luo, H. Yu, F. Hu, T. Liu, X. Cheng, R. Zheng, Y. Bai, M. Shui and J. Shu, *Chem. Eng. J.*, 2020, **380**, 122557.
7 Z. Hao, X. Shi, Z. Yang, L. Li and S.-L. Chou, *Adv. Funct. Mater.*, 2022, **32**, 2208093.
8 H. He, H. Zhang, D. Huang, W. Kuang, X. Li, J. Hao, Z. Guo and C. Zhang, *Adv. Mater.*, 2022, **34**, 2200397.
9 Y. Chao, Y. Han, Z. Chen, D. Chu, Q. Xu, G. Wallace and C. Wang, *Adv. Sci.*, 2023, 2305558.
10 S. Li, C. Huang, L. Gao, Q. Shen, P. Li, X. Qu, L. Jiao, Y. Liu, S. Li, C. Huang, L. Gao, Q. Shen, P. Li, X. Qu, Y. Liu and L. Jiao, *Angew. Chem., Int. Ed.*, 2022, **61**, e202211478.
11 S. Li, X. Zhao, T. Wang, J. Wu, X. Xu, P. Li, X. Ji, H. Hou, X. Qu, L. Jiao and Y. Liu, *Angew. Chem., Int. Ed.*, 2024, **63**, e202320075.
12 G. Lin, Q. Ju, X. Guo, W. Zhao, S. Adimi, J. Ye, Q. Bi, J. Wang, M. Yang and F. Huang, *Adv. Mater.*, 2021, **33**, 2007509.
13 H. Xia, L. Zan, P. Yuan, G. Qu, H. Dong, Y. Wei, Y. Yu, Z. Wei, W. Yan, J. Hu, D. Deng and J. Zhang, *Angew. Chem., Int. Ed.*, 2023, **62**, e202218282.
14 Y. Zhang, J. Wang, L. Shan, B. Han, Q. Gao, Z. Cai, C. Zhou, X. Tian, R. Sun and L. Mai, *Adv. Energy Mater.*, 2023, 2303464.
15 G. Fang, Q. Wang, J. Zhou, Y. Lei, Z. Chen, Z. Wang, A. Pan and S. Liang, *ACS Nano*, 2019, **13**, 5635–5645.
16 J. Cheng, Z. Niu, Z. Zhao, X. Pei, S. Zhang, H. Wang, D. Li and Z. Guo, *Adv. Energy Mater.*, 2023, **13**, 2203248.
17 X. Xie, X. Ma, Z. Yin, H. Tong, H. Jiang, Z. Ding and L. Zhou, *Chem. Eng. J.*, 2022, **446**, 137366.
18 Y. Li, Z. Yuan, D. Li, J. Li, Y. Zhang, M. Wang, G. Li, L. Wang and W. Han, *ACS Nano*, 2024, **18**, 4733–4745.
19 Y. Xiao, X. Zhao, X. Wang, D. Su, S. Bai, W. Chen, S. Fang, L. Zhou, H.-M. Cheng and F. Li, *Adv. Energy Mater.*, 2020, **10**, 2000666.
20 H. Peng, W. Miao, S. Cui, Z. Liu, X. Wang, B. Tao, W. Hou, Z. Zhang and G. Ma, *Chem. Eng. J.*, 2024, **487**, 150701.
21 P. Y. Deng, K. K. Wang, H. Y. Sung, W. W. Wu and H. J. Wu, *Cell Rep. Phys. Sci.*, 2023, **4**, 101413.
22 F. Jia, S. Zhang, X. Zhang, X. Peng, H. Zhang and Y. Xiang, *Chem.–Eur. J.*, 2014, **20**, 15941–15946.
23 Y. Fang, D. Luan, X. Wen, D. Lou, Y. J. Fang, D. Y. Luan and X. W. Lou, *Adv. Mater.*, 2020, **32**, 2002976.
24 C. Wang, J. Lu, H. Tong, S. Wu, D. Wang, B. Liu, L. Cheng, Z. Lin, L. Hu, H. Wang, W. Zhang and Q. Chen, *Nano Res.*, 2021, **14**, 3545–3551.
25 S. Li, Y. Liu, X. Zhao, Q. Shen, W. Zhao, Q. Tan, N. Zhang, P. Li, L. Jiao and X. Qu, *Adv. Mater.*, 2021, **33**, 2007480.
26 L. Yue, D. Wang, Z. Wu, W. Zhao, Y. Ren, L. Zhang, B. Zhong, N. Li, B. Tang, Q. Liu, Y. Luo, A. M. Asiri, X. Guo and X. Sun, *Chem. Eng. J.*, 2022, **433**, 134477.
27 Y. Yin, Y. Zhang, T. Gao, T. Yao, X. Zhang, J. Han, X. Wang, Z. Zhang, P. Xu, P. Zhang, X. Cao, B. Song, S. Jin, Y. Yin, Y. Zhang, X. Zhang, J. Han, T. Yao, X. Wang, B. Song, Z. Zhang, P. Xu, P. Zhang, X. Cao and S. Jin, *Adv. Mater.*, 2017, **29**, 1700311.
28 Z. Liu, Y. Tian, S. Li, L. Wang, B. Han, X. Cui and Q. Xu, *Adv. Funct. Mater.*, 2023, **33**, 2301994.
29 K.-A. N. Duerloo, Y. Li and E. J. Reed, *Nat. Commun.*, 2014, **5**, 4214.
30 P. Yan, L. Ji, X. Liu, Q. Guan, J. Guo, Y. Shen, H. Zhang, W. Wei, X. Cui and Q. Xu, *Nano Energy*, 2021, **86**, 106139.
31 R. Zhou, Y. Huang, J. Zhou, H. Niu, L. Wan, Y. Li, J. Xu and J. Xu, *Dalton Trans.*, 2018, **47**, 16587–16595.
32 Y. Yu, G.-H. Nam, Q. He, X.-J. Wu, K. Zhang, Z. Yang, J. Chen, Q. Ma, M. Zhao, Z. Liu, F.-R. Ran, X. Wang, H. Li, X. Huang, B. Li, Q. Xiong, Q. Zhang, Z. Liu, L. Gu, Y. Du, W. Huang and H. Zhang, *Nat. Chem.*, 2018, **10**, 638–643.
33 G. Zhu, D. Luo, X. Chen, J. Yang and H. Zhang, *ACS Nano*, 2023, **17**, 20850–20874.
34 Z. Li, L. Yu, X. Tao, Y. Li, L. Zhang, X. He, Y. Chen, S. Xiong, W. Hu, J. Li, J. Wang, H. Jin and S. Wang, *Small*, 2023, 2304124.
35 S. Chong, X. Wei, Y. Wu, L. Sun, C. Shu, Q. Lu, Y. Hu, G. Cao and W. Huang, *ACS Appl. Mater. Interfaces*, 2021, **13**, 13158–13169.
36 X. Liu, Z. Niu, Y. Xu, Z. Zhao, C. Li, Y. Yi, H. Guan, S. Zhang, X. Pei and D. Li, *Chem. Eng. J.*, 2022, **430**, 133176.
37 X. Zhang, Y.-Y. Zhang, Y. Zhang, W.-J. Jiang, Q.-H. Zhang, Y.-G. Yang, L. Gu, J.-S. Hu and L.-J. Wan, *Small Methods*, 2019, **3**, 1800317.
38 Y. Zhang, S. Deng, Y. Shen, B. Liu, G. Pan, Q. Liu, X. Wang, Y. Wang, X. Xia and J. Tu, *ChemSusChem*, 2020, **13**, 1575–1581.
39 Y. R. Pei, H. Y. Zhou, M. Zhao, J. C. Li, X. Ge, W. Zhang, C. C. Yang and Q. Jiang, *Carbon Energy*, 2023, e374.
40 R. Jin, X. Liu, L. Yang, G. Li and S. Gao, *Electrochim. Acta*, 2018, **259**, 841–849.
41 Y. Chao, R. Jalili, Y. Ge, C. Wang, T. Zheng, K. Shu and G. G. Wallace, *Adv. Funct. Mater.*, 2017, **27**, 1700234.
42 Y. Hoe Seon, Y. Chan Kang and J. S. Cho, *Chem. Eng. J.*, 2021, **425**, 129051.
43 N. Shi, Y. Chu, B. Xi, M. Huang, W. Chen, B. Duan, C. Zhang, J. Feng and S. Xiong, *Adv. Energy Mater.*, 2020, **10**, 2002298.
44 Y. Liu, Y. Yi, Z. Niu, S. Wei, X. Pei, Y. Fu, J. Wang, M. Ge, Z. Liu and D. Li, *ACS Appl. Mater. Interfaces*, 2022, **14**, 6926–6936.
45 L. Zhang, H. Dong, H. Wei, E. H. Ang, J. Yang, X. Miao, H. Geng and X. Zuo, *J. Power Sources*, 2021, **506**, 230216.
46 S. Li, H. Zhang, Y. Cao, S. Zhang, Z. Liu, C. Yang, Y. Wang and B. Wan, *Nanoscale*, 2023, **15**, 5655–5664.
47 J. Feng, S. hua Luo, P. wei Li, Y. cheng Lin, L. Zhang, Q. Wang and Y. hui Zhang, *Appl. Surf. Sci.*, 2023, **619**, 156775.
48 B. Wang, J. Y. Xue, F. L. Li, H. Geng and J. P. Lang, *ChemSusChem*, 2021, **14**, 5304–5310.
49 Q. Sun, Y. Wen, S. Jiang, X. Li, Z. Yao, T. Liu, S. Shen and Y. Yang, *J. Alloys Compd.*, 2023, **944**, 169157.

50 J. Chen, A. Pan, Y. Wang, X. Cao, W. Zhang, X. Kong, Q. Su, J. Lin, G. Cao and S. Liang, *Energy Storage Materials*, 2019, **21**, 97–106.
51 Z. Yan, L. Zhao, Y. Liang, L. Zhang, H. Liu, Z. Zhu, Y. Wang and S. L. Chou, *Carbon Energy*, 2022, **4**, 586–597.
52 Y. Liang, Z. Wang, Z. Xu, S. Li, H. Luo, C. Xu and X. Cui, *Appl. Surf. Sci.*, 2024, **651**, 159234.
53 M. Yousaf, Y. Wang, Y. Chen, Z. Wang, A. Firdous, Z. Ali, N. Mahmood, R. Zou, S. Guo and R. P. S. Han, *Adv. Energy Mater.*, 2019, **9**, 1900567.
54 F. Zhou, S. Xin, H. W. Liang, L. T. Song and S. H. Yu, *Angew. Chem., Int. Ed.*, 2014, **53**, 11552–11556.
55 L. Wang, J. Światowska, S. Dai, M. Cao, Z. Zhong, Y. Shen and M. Wang, *Mater. Today Energy*, 2019, **11**, 46–60.
56 X. Y. Yu and X. W. (David) Lou, *Adv. Energy Mater.*, 2018, **8**, 1701592.
57 J. B. Cook, H.-S. Kim, Y. Yan, J. S. Ko, S. Robbennolt, B. Dunn and S. H. Tolbert, *Adv. Energy Mater.*, 2016, **6**, 1501937.